sustainability

Article

Numerical Analysis of the Impact Parameters on the Dynamic Response of a Submerged Floating Tunnel under Coupling Waves and Flows

Wanhai Xu *, Zhiyou Song, Guangjun Liu and Yumeng Sun

State Key Laboratory of Hydraulic Engineering Simulation and Safety, Tianjin University, Tianjin 300350, China; songzhiyou@tju.edu.cn (Z.S.); lgj20220825@tju.edu.cn (G.L.); sym1234567@tju.edu.cn (Y.S.)
* Correspondence: xuwanhai@tju.edu.cn

Abstract: The Submerged Floating Tunnel (SFT) is a highly promising cross-sea transportation structure. Due to its body being suspended in water, waves and flows are the primary environmental loads it encounters. Existing numerical simulations have been based on potential flow theory, which fails to fully consider shear forces and the nonlinear characteristics of the flow field. To overcome this limitation, the Computational Fluid Dynamics (CFD) approach, relying on solving the Navier-Stokes equations, can be employed. In this study, we establish a CFD model for the SFT and analyze the impact mechanisms of wave-flow coupling on its dynamic response, considering parameters such as wave height, flow velocity, wave direction, and flow direction. With increasing wave height, the acceleration, mooring tension, and heave amplitude of the SFT significantly increase, and the nonlinear characteristics of its dynamic response become more pronounced. For example, when wave height, H_i, increases from 0.046 m to 0.138 m, the maximum value of dimensionless heave, δ_z/H_i, increases from 0.075 to 0.284, nearly quadrupling in magnitude. When waves and flows propagate in the same direction, the heave amplitude of the SFT increases compared to the case with waves acting alone, while sway and roll amplitudes decrease. Under conditions of higher flow velocity, the SFT displaces significantly along the direction of flow and water depth, deviating significantly from its original equilibrium position. At this point, the tunnel primarily experiences periodic forces due to vortex shedding, and the anchor chain on the downstream side remains slack. In scenarios where waves and flows propagate in opposite directions, both the maximum acceleration and mooring tension of the SFT increase significantly. For instance, the onshore tension of the cable, F_{on}, increases by 36%, while the offshore tension, F_{off}, increases by 89%.

Keywords: submerged floating tunnel; wave-flow coupling; CFD; dynamic response; mooring tension

Citation: Xu, W.; Song, Z.; Liu, G.; Sun, Y. Numerical Analysis of the Impact Parameters on the Dynamic Response of a Submerged Floating Tunnel under Coupling Waves and Flows. *Sustainability* **2023**, *15*, 15241. https://doi.org/10.3390/su152115241

Academic Editor: Yefei Bai

Received: 3 September 2023
Revised: 18 October 2023
Accepted: 20 October 2023
Published: 25 October 2023

1. Introduction

A Submerged Floating Tunnel (SFT) is generally suspended 20–50 m below the water surface and can cross the two sides of the strait. It is recognized as the most promising form of cross-sea transportation in the 21st century [1]. According to different supporting systems, submerged floating tunnels are divided into pontoon type, pier type, anchor cable type, and free type [2,3]. The SFT is mainly affected by waves and currents, so the study of its hydrodynamic response is the key to the safe design of a submerged floating tunnel structure.

Theoretical analysis methods can quickly predict the response features of an SFT under hydrodynamic loading. Fan et al. [4] studied the resonance of a single-span SFT undergoing vortex-shedding. They simplified the tunnel structure as a simply supported Euler–Bernoulli beam at both ends, calculated the fluid damping and drag force using the Morison formula, and found that in a specific range of incoming flow velocities, the fluid–structure coupling effect and nonlinear characteristics have a significant impact on the structural response. Ge et al. [5] solved the wave field and the interaction between the wave and the SFT based on the potential flow theory and the boundary element method, respectively. They used the prototype design parameters of the SFT in Qiandao Lake as a case to carry out systematic analysis. Numerous scholars have conducted research on the dynamic response of the SFT under wave or current loads based on theoretical analysis methods [6–8]. Although the theoretical analysis has high computational efficiency, the many simplification conditions limit its application. For example, the potential flow theory neglects the fluid viscosity and cannot accurately calculate the viscous shearing force. The Morison formula can only calculate the force on small-scale components [9]. In addition, it is difficult to address the nonlinear problem of a free liquid surface through theoretical analysis.

The model test is an important method for investigating the SFT's dynamic response. Many researchers have studied the SFTs' response under the action of waves, flows, or wave-flow coupling [10–13]. They mainly focused on the motion of the six degrees of freedom of the SFT, tunnel pipe acceleration, anchor cable tension, and tunnel pipe section pressure. The dynamic response of the SFT is mainly controlled by two sets of parameters. One set corresponds to the loads, including wave height, wave period, and incoming flow velocity. The other set pertains to coefficients characterizing the SFT system, including submersion depth, weight-to-buoyancy ratio, and cable inclination angle. These two sets of parameters have been the central focus of previous experimental investigations. Model tests also have deficiencies; for example, it is difficult to simulate large and steep waves, the test cycle is long, and the cost is high.

With the development of computer performance, numerical simulation has gradually become another important means to study the dynamic response of SFTs. Yang et al. [14] established a finite element model (FEM) of a SFT and anchor cables based on AQWA. They studied the dynamic response of anchor cables under the action of waves and flow and found that regular waves and uniform flow caused periodic motion of the structure and large displacement and low-frequency movement. Zou et al. [15] numerically studied the dynamic response characteristics of the SFT-anchor cable coupling system and found that the tube motion response increased with increasing wave height and mooring angle. Luo et al. [16] numerically solved the simplified differential equations for the tunnel pipe and anchor cable system. The response amplitude of the SFT and the anchor cable tension increase with increasing wave height and wave period and decrease with increasing submersion depth. Zou et al. [17] used the one-way coupling method of CFD and FEM to study the response of SFT in extreme sea conditions. They pointed out that waves with large wave heights and large periods could avoid exciting the first-order dominant mode of SFT. Chen et al. [18] numerically studied the nonlinear interaction between waves and SFTs. They proposed that an appropriate buoyancy-to-weight ratio could prevent the large movement of SFTs under adverse wave conditions. Peng et al. [19] established a CFD model of the interaction between waves and SFTs. They found that the CFD model based on solving the Navier–Stokes equations could fully consider processes such as the nonlinearity of the flow field, vortex formation, boundary layer separation, and wave breaking.

In summary, a large number of researchers have numerically studied the dynamic response of a SFT under the action of waves or flows alone, but there are relatively few studies under the action of wave-flow coupling. In addition, many numerical simulations are based on potential flow theory, which cannot consider the force generated by vortex shedding. In this paper, a CFD model of an SFT is established, which can not only calculate the drag force and lift force caused by vortex shedding by considering the fluid viscosity but also capture nonlinear load characteristics such as free liquid surface reversal and breakage. SFTs in the actual marine environment are generally subjected to the combined action of wave and flow loads, and the directions of wave propagation and flow are generally not perfectly aligned. Hence, when investigating the coupling effects of waves and flows, the impacts of factors such as wave height and flow velocity, as well as the directions of wave and flow propagation, bear enhanced practical significance for the dynamic response of SFTs.

2. Numerical Model

The commercial CFD software STARCCM+ V2206 is utilized for numerical simulations. The fluid domain is discretized based on the finite volume method. In the discretized control volume, the governing equations of fluid flow are converted to algebraic equations. The algebraic equations are iteratively solved, combined with the boundary conditions, and initial conditions to obtain the numerical solution of the real flow [20]. The compressibility of fluid is not considered, and the controlling equations of fluid flow are the time-averaged continuity equation and Reynolds equation (RANS) shown in Equations (1) and (2):

$$\frac{\partial \overline{u_i}}{\partial x_i} = 0 \tag{1}$$

$$\rho\left[\frac{\partial \overline{u_i}}{\partial t} + \frac{\partial\left(\overline{u_i u_j}\right)}{\partial x_j}\right] = -\frac{\partial \overline{p}}{\partial x_i} + \mu \nabla^2 \overline{u_i} + \frac{\partial}{\partial x_j}\left(-\rho \overline{u'_i u'_j}\right) + \overline{\rho g_i} \tag{2}$$

where $\overline{u_i}$ is the time-average value of velocity, $\overline{p}$ is the time-average value of pressure, μ is the dynamic viscosity of the fluid, ρ is the density of the fluid, $\overline{\rho g_i}$ is the time-average of body force, g_i is the gravitational acceleration vector, and $-\rho\overline{u'_i u'_j}$ is the Reynolds stress term and a second-order tensor. The Reynolds stress term appears in Equation (2), and the governing equations of fluid motion are not closed. The k-ε turbulence model is chosen as the supplementary equation to establish the relationship between the Reynolds stress and the average velocity, making Equations (1) and (2) closed and solvable. The Eulerian multiphase flow model was used to create the air phase and the water phase, and the volume-of-fluid (VOF) method captured the interface of the two phases. The left and right boundaries of the calculation domain are set as “velocity inlet” boundaries. This boundary condition can simulate the real physical wave-making process by pushing the plate. The wave parameters are specified based on the intermediate water depth wave theory, and the wave propagation direction is from the left side to the right side. With the “wall” boundary at the bottom and the SFT, this is equivalent to a no-slip wall boundary condition. The “pressure outlet” boundary is at the top. The front and back sides were set as “symmetry planes”, and this boundary condition made the velocity gradient normal to the plane zero, thus converting the simulation problem into a 2D problem. At the same time, the “wave force” option is used on the “velocity inlet” boundary, and the “wave force length” is set to twice the wavelength. This method of wave mitigation allows the selection of a smaller computational domain size and improves computational efficiency [21]. The selection of boundary conditions and computation domain size are shown in Figure 1a. The fluid calculation domain is subdivided based on the “trimmed mesh”. Due to the large magnitude of rigid body motion in the SFT, the overset mesh method is chosen to discretize the calculation domain around the SFT. To ensure the accuracy of grid interpolation, the mesh sizes of the background region and the overlapping region should be approximately matched. Near the water surface, significant interactions occur between waves and structures. Therefore, the grid in the vicinity of the water surface needs to be refined. The refinement criterion is to divide a unit wavelength into 80 grids and a unit wave height into 20 grids. Due to the viscosity of the fluid, there is a boundary layer with a certain thickness on the surface of the SFT. In the boundary layer, the velocity gradient is relatively large, and the shear stress cannot be ignored. Therefore, the “prismatic layer mesh” was used for the SFT surface to accurately calculate the viscous shear force. Figure 1b shows the meshing on the cross-section perpendicular to the y-axis. The “DFBI” module in STARCCM+ can solve the force and movement of the SFT, and the catenary option under this module can be used to establish the numerical calculation model of the SFT and anchor chain system [22].

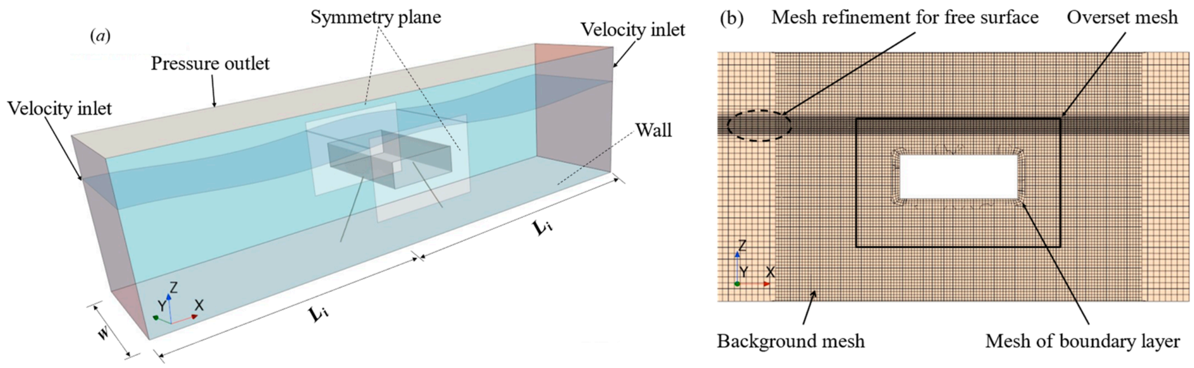

Figure 1. Setting of boundary conditions and discretization of grids. (**a**) Boundary conditions (**b**) Discretization of grids.

3. Model Validation

Three sets of grids with different sizes were established, with dimensions of 0.226 m, 0.16 m, and 0.113 m, corresponding to grid quantities of 280,000, 790,000, and 2,370,000, respectively. The comparison shows that the calculation on the fine mesh shows that the dimensionless sway amplitude (δ_x/H_i), the dimensionless heave amplitude (δ_z/H_i), and the dimensionless pitch amplitude ($\alpha B/(2H_i)$) were all larger and closer to the experimental values. The deviations between the calculated values of δ_x/H_i, δ_z/H_i, and $\alpha B/(2H_i)$ obtained from fine and moderate grids are 2.6%, 9.5%, and 6.5%, respectively, as shown in Table 1. Further refining the grid based on the moderate grid has a significant impact only on δ_z/H_i. Moreover, the deviation between the calculated δ_z/H_i obtained from the moderate grid size and the experimental value is already relatively small. Considering both computational accuracy and efficiency, the subsequent calculations will adopt the moderate grid size as the standard for grid partitioning.

Table 1. Calculation results for different grid sizes.

Grid Level	Grid Number/Million	δ_z/H_i	$\alpha B/(2H_i)$	δ_x/H_i
Coarse	0.28	0.038	0.289	0.341
Moderate	0.79	0.042	0.294	0.345
Fine	2.37	0.046	0.313	0.354

The model experiment involves an SFT with a rectangular cross-section. The relevant parameters of the SFT are provided in Table 2. Here, B, W, and h denote the SFT model's length, width, and height, respectively. A series of laboratory experiments were conducted within a 2D glass-walled wave flume situated at the Coastal and Ocean Engineering Laboratory, Department of Civil Engineering, Nagoya University, Japan. The wave tank's dimensions are 30 m in length, 0.7 m in width, and 0.9 m in depth. The wave channel's bottom is flat, and a piston-type wave paddle is installed at the closed end of the wave flume to generate waves. On the opposite end of the wave flume, a wave absorber constructed of a rubble mound is employed to minimize the impact of reflected waves. Positioned midway between the wave maker and the wave absorber is a model breakwater that spans the entire width of the wave tank. Consequently, the flow can be treated as two-dimensional. Further details about the experiment can be found in Peng et al. [19]. The model has a mass of m = 28.6 kg, and the moment of inertia is I = 0.435 kg m^2. The immersion depth of the model is ds = 0.102 m. The parameters of the model experiment are outlined in Table 3. In this table, T_i, H_i, and L_i represent the wave period, wave height, and wavelength, respectively. The variable d stands for the water tank depth, while β indicates the inclination angle of the anchor cable and F_i corresponds to the initial tension of the anchor cable. In the model experiment of Peng et al. [19], a total of four anchor cables were symmetrically arranged. The numerical computational model incorporates two anchor chains along the mid-longitudinal section. Subsequently, the forces calculated for each anchor cable were equivalently distributed onto the two anchor chains, achieving consistency with the model experiment. The side view of the model test is illustrated in Figure 2.

Table 2. Structural parameters of SFT with a rectangular cross-section.

B/m	W/m	h/m	m/kg	I/kg m^2
0.4	0.68	0.15	28.6	0.435

Table 3. Relevant parameters of the model experiment.

T_i/s	H_i/m	ds/m	L_i/m	d/m	β/°	F_i/N
1	0.046	0.102	1.575	0.6	60	34.51
1	0.046	0.102	1.575	0.6	60	35.04

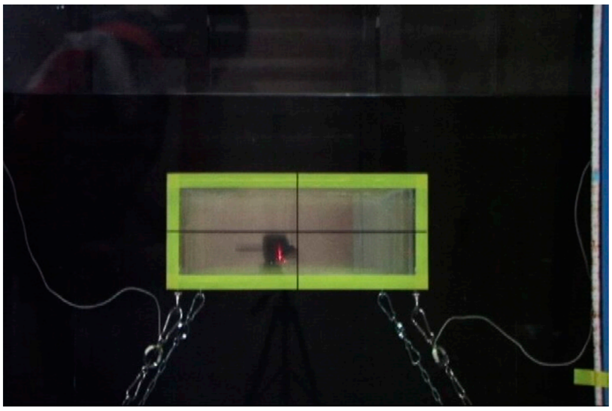

Figure 2. The side view of the model test. Reprinted/adapted with permission from Ref. [19]. 2013, Peng et al.

Figure 3 presents a comparison between numerical results and experimental data. In the figures, “EXP” represents the outcomes from the model experiment, while “CFD” signifies the results obtained through numerical computation. Here, “a_x” and “a_z” stand for the lateral and vertical accelerations of the model, while “F_{off}” and “F_{on}” correspond to the offshore and onshore tensions of the anchor cable. In accordance with Figure 3, the time series of various response values of the SFT obtained through numerical simulations exhibit good agreement with the model experiment. Specifically, the amplitude values of SFT’s pitch, roll, and lateral acceleration obtained through numerical solutions are slightly lower than those observed in the model test, whereas sway, vertical acceleration, and the offshore and onshore tensions of the anchor cable are observed to be a little larger than the model test values. Perhaps modifying the added mass coefficient during the numerical simulation process could yield results that are more closely aligned with the model experiments. However, due to the lack of clear experimental guidance on how large the added mass coefficient should be, we did not adjust the added mass coefficient. Furthermore, the nonlinear response characteristics can be effectively captured through numerical simulations. Because the CFD method not only considers the fluid’s viscosity but also accounts for nonlinear loads caused by wave breaking or slamming processes, as shown in Figure 4. These nonlinear loads, such as second-order wave forces and slamming forces, have a significant impact on the response of the SFT. In the experiment of Peng et al. [19], the SFT is connected via a bottom fixed end and steel chains. The connection between the steel chain end and the SFT is close to a hinge joint, allowing rotation between the two components. Conversely, in the numerical computations, the anchor chain is fixedly connected to the SFT. This difference in connection might contribute to the observed deviations in the corresponding response values.

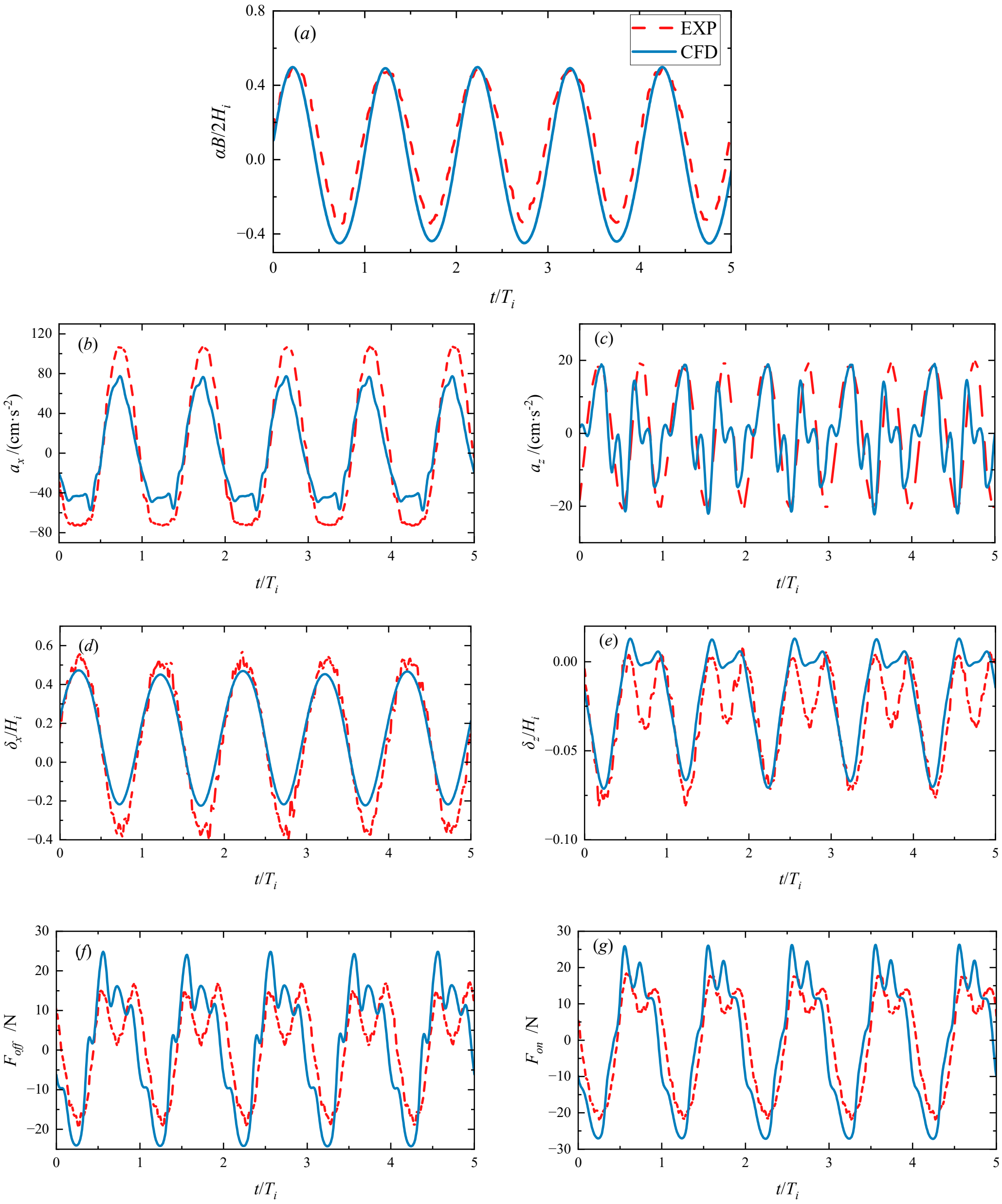

Figure 3. Comparison between the numerical results and the experimental results. (**a**) Roll of the SFT (**b**) Horizontal directional acceleration of the SFT (**c**) Vertical directional acceleration of the SFT (**d**) Sway of the SFT (**e**) Heave of the SFT (**f**) Offshore tension of the anchor cable (**g**) Onshore tension of the anchor cable.

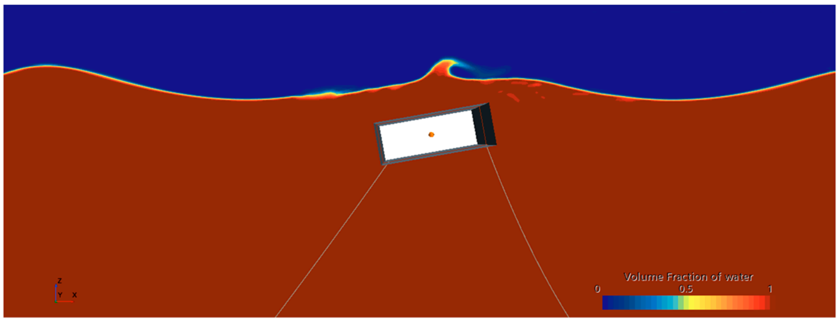

Figure 4. Wave curling and wave breaking.

To further validate the accuracy of the numerical model presented in this paper, the dynamic responses of a circular cross-section SFT model under regular wave conditions were calculated and compared with relevant model tests and numerical simulation results, as shown in Figure 5. The numerical simulation results by Peng [19] were also presented in the figure. The relevant parameters for the model test are listed in Table 3. In comparison to the model test conditions for a rectangular cross-section tunnel, the initial tensile forces of the mooring line slightly increased to $F_i = 35.04$ N. The relevant model parameters for the circular cross-section SFT are presented in Table 4, where R represents the radius of the circle. As evident from Figure 5, the non-dimensional roll, F_{off}, and F_{on} responses of the circular cross-section SFT obtained from our numerical simulations closely match the model test results and Peng's numerical simulation results. The respective response amplitudes exhibit errors of 14%, 8%, and 3.8% when compared to the model test. The calculated dimensionless sway amplitude is even closer to the model test results than Peng's calculations, with an error of 2.5%. However, both our numerical calculations and Peng's results yield significantly lower heave motion amplitudes compared to the model test, and these oscillations exhibit a frequency close to the wave period without displaying the high-frequency oscillations observed in the model test.

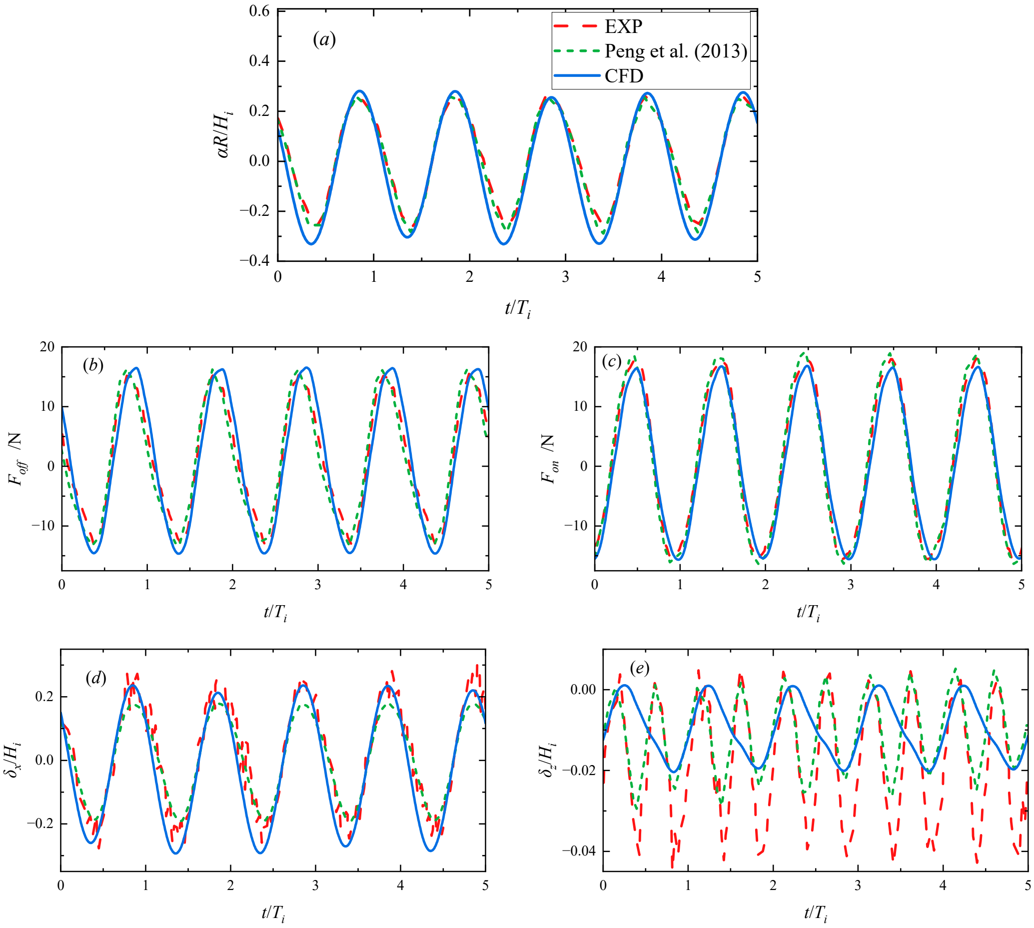

Figure 5. Comparison between the numerical results and the experimental results. Reprinted/adapted with permission from Ref. [19]. 2013, Peng et al. (**a**) Roll of the SFT (**b**) Offshore tension of the anchor cable (**c**) Onshore tension of the anchor cable (**d**) Sway of the SFT (**e**) Heave of the SFT.

Table 4. Structural parameters of SFT with a circular cross-section.

R/m	W/m	m/kg	I/kg m^2
0.125	0.68	21	0.164

4. Response of SFT under Wave-Flow Coupling

In this section, the response of the SFT is analyzed under waves and flows. In the case of isolated wave loading, the impact of wave height on the SFT response is examined. Under the combined influence of waves and flows, the effects of various parameters, including wave height, current velocity, wave propagation direction, and current propagation direction, on the SFT response are individually investigated. The water depth has an influence on the motion of water particles within waves. To study the impact of wave height, the water depth is increased to d = 0.9 m, at which point $d/L_i > 1/2$, satisfying the conditions for deep-water waves.

4.1. Response under a Regular Wave

Parameters such as L_i, ds, and β are consistent with the model experiment of Peng et al. [19]. The influence of wave height, H_i, on the response of the SFT is analyzed. The parameters of the wave load are presented in Table 5.

Table 5. Wave parameters.

d/m	H_i/m	L_i/m	H_i/L_i
0.9	0.046	1.575	0.029
0.9	0.092	1.575	0.058
0.9	0.138	1.575	0.088

With an increase in wave height, the maximum values of a_x, a_z, F_{off}, F_{on}, and δ_z/H_i all notably escalate. As H_i increases from 0.046 m to 0.138 m, the maximum value of δ_z/H_i increases from 0.075 to 0.284, nearly quadrupling. This is accompanied by an amplification of the nonlinear characteristics in the time history curves of each response. This phenomenon could be attributed to the heightened wave-induced fluctuating pressure at the same immersion depth as wave height increases. This leads to an augmentation in the wave forces acting on the surface of the SFT. Furthermore, the interaction between the SFT and the waves intensifies as the wave height increases, resulting in more prominent curling and breaking of the waves. Consequently, the nonlinear attributes of the wave loads become more pronounced. Simultaneously, the inherent nonlinearity of the wave loads (represented by the steepness parameter H_i/L_i) also magnifies with increasing wave height. During changes in wave height, the dimensionless lateral sway, δ_x/H_i, exhibits no significant variation. However, the maximum value of the dimensionless pitch motion, $\alpha B/(2H_i)$, initially increases and then decreases with rising wave height, as illustrated in Figures 6 and 7.

4.2. Response under Wave-Flow Coupling

The wave parameters are provided in Table 5. Additionally, under the presence of incoming flow conditions, the analysis of wave height's influence maintains a fixed flow velocity of 0.175 m/s, while the analysis of flow velocity's influence maintains a fixed wave height of 0.092 m. Lastly, by fixing the wave height at 0.092 m and the flow velocity at 0.175 m/s, the response characteristics of the SFT are investigated under varying wave-flow propagation directions.

4.2.1. Influence of Wave Height with the Same Propagation Direction of Waves and Flows

When waves propagate in the same direction as the current and with a fixed current velocity, the effect of wave height on the SFT is similar to the case of wave load. As wave height increases, the maximum values of a_x, a_z, F_{off}, F_{on}, and δ_z/H_i increase, while those of δ_x/H_i and $\alpha B/(2H_i)$ decrease. By comparing Figures 6 and 8, it can be observed that when waves and currents are coupled, the δ_z/H_i of SFT increases at any given wave height compared to the case of wave loads alone. Meanwhile, the magnitudes of δ_x/H_i and $\alpha B/(2H_i)$ oscillations decrease compared to the case of wave loads. The presence of steady currents subjects the SFT to drag forces along the flow direction and lift forces in the vertical flow direction. These forces combine with the wave forces, resulting in an increased vertical net force on the SFT and a decreased lateral net force and torsional moment. Additionally, the equilibrium position of the lateral oscillation of the SFT shifts along the wave and current propagation directions. The magnitude of this shift is influenced by wave height—the larger the wave height, the smaller the shift distance. Furthermore, as wave height increases, the lateral oscillation amplitude significantly diminishes. When wave height increases from 0.046 m to 0.138 m, the amplitude decreases from 0.299 to 0.181, a reduction of approximately 39%. Similarly, the SFT undergoes a certain angle of rotation against the incoming flow, followed by a periodic rotational motion in its rotated position. Likewise, as the wave height increases, the counterclockwise rotation angle diminishes. When wave height increases from 0.046 m to 0.138 m, the $\alpha B/(2H_i)$ amplitude decreases from 0.255 to about 0.1, a decrease of around 60%. With increasing wave height, the nonlinear characteristics of the pitch motion time history of the SFT become more pronounced. When H_i = 0.138 m, the pitch motion exhibits no periodic motion characteristics, as depicted in Figure 8.

4.2.2. Influence of Flow Velocity with Same Propagation Direction of Waves and Flows

When waves propagate along with the flow, as the flow velocity increases from 0.088 m/s to 0.349 m/s, the maximum values of a_x, a_z, F_{on}, and F_{off} for the SFT notably decrease. This phenomenon can be attributed to the fact that as the flow velocity increases, the SFT moves a greater distance in both the flow direction and the water depth direction. Additionally, the angle of counterclockwise rotation against the flow direction also increases. As the flow velocity surpasses a certain threshold, the immersion depth of the SFT becomes larger than half the wavelength. At this point, the wave load on the SFT becomes negligible, and the motion of the SFT is governed by the lift and drag forces associated with vortex shedding. Consequently, the amplitude of motion becomes smaller, and the SFT deviates significantly from its original equilibrium position. When the flow velocity reaches 0.349 m/s, the anchor chain facing the flow direction remains under tension, while the other side of the anchor chain remains completely slack without tension. Under these circumstances, the period and amplitude of the pitch motion of the SFT are mainly controlled by vortex shedding, as shown in Figure 9. It can be observed that with higher flow velocities, the lift generated by vortex shedding on the surface of SFT is sufficient to induce significant heave and pitch oscillations, while the relatively smaller drag results in a smaller amplitude of sway motion, as illustrated in Figure 10. In the context of wave-flow coupling, it is difficult to form stable vortex shedding around the SFT in regions where fluid particles undergo a reciprocal oscillatory motion. However, when the incoming flow velocity is relatively high and the distance over which the SFT moves toward the seabed is significant, the vibrational motion of water particles becomes negligible, and stable incoming flows are more likely to generate vortex shedding. Therefore, Figure 8 may not represent a universal phenomenon. This phenomenon is expected to occur more readily under conditions of higher incoming flow velocities and when SFT moves away from the oscillatory water particle region.

4.2.3. Opposite Propagation Directions of Waves and Flows

When waves and flows propagate in the same direction ($\theta = 0°$) and in opposite directions ($\theta = 180°$), as discerned from Figure 11, it becomes evident that, for a fixed wave height and flow velocity, when waves and flows propagate in reverse, the maximum values of a_x, a_z, F_{on}, and F_{off} for the SFT exhibit a notable increase. In comparison to the scenario of co-propagation of waves and flows, these values escalate by approximately 27.6%, 130%, 36%, and 89%, respectively. The dimensionless sway amplitude δ_x/H_i and pitch amplitude $\alpha B/(2H_i)$ also undergo increments of approximately 66.2% and 82.6%, respectively. However, the heave motion δ_z/H_i of the SFT experiences a significant reduction of around 39.4%. This trend is contrary to the anticipated effects of the Doppler effect, where waves propagating against the flow are expected to exhibit heightened amplitudes, while those propagating in the same direction are anticipated to display diminished amplitudes. Interestingly, when waves and flows propagate in the same direction, δ_z/H_i increases, whereas in the case of reverse propagation, δ_z/H_i experiences a notable decrease. The patterns of δ_z/H_i variations with wave height diverge from those observed when wave loads act in isolation. Under the combined influence of wave and flow interactions, the forces acting upon the SFT are a composite of flow-induced loads (drag and lift) and wave-induced loads. Alterations in the directions of wave and flow propagation substantially modify the distribution of forces on the SFT. During the co-propagation of waves and flows, the equilibrium positions of the sway and pitch motion of the SFT closely resemble the initial equilibrium position. This contrasts with the situation when wave and flow propagation directions are identical. Moreover, during reverse propagation, both anchor chain tension and the acceleration of the SFT exhibit significant increments, necessitating due consideration in the assessment of structural strength.

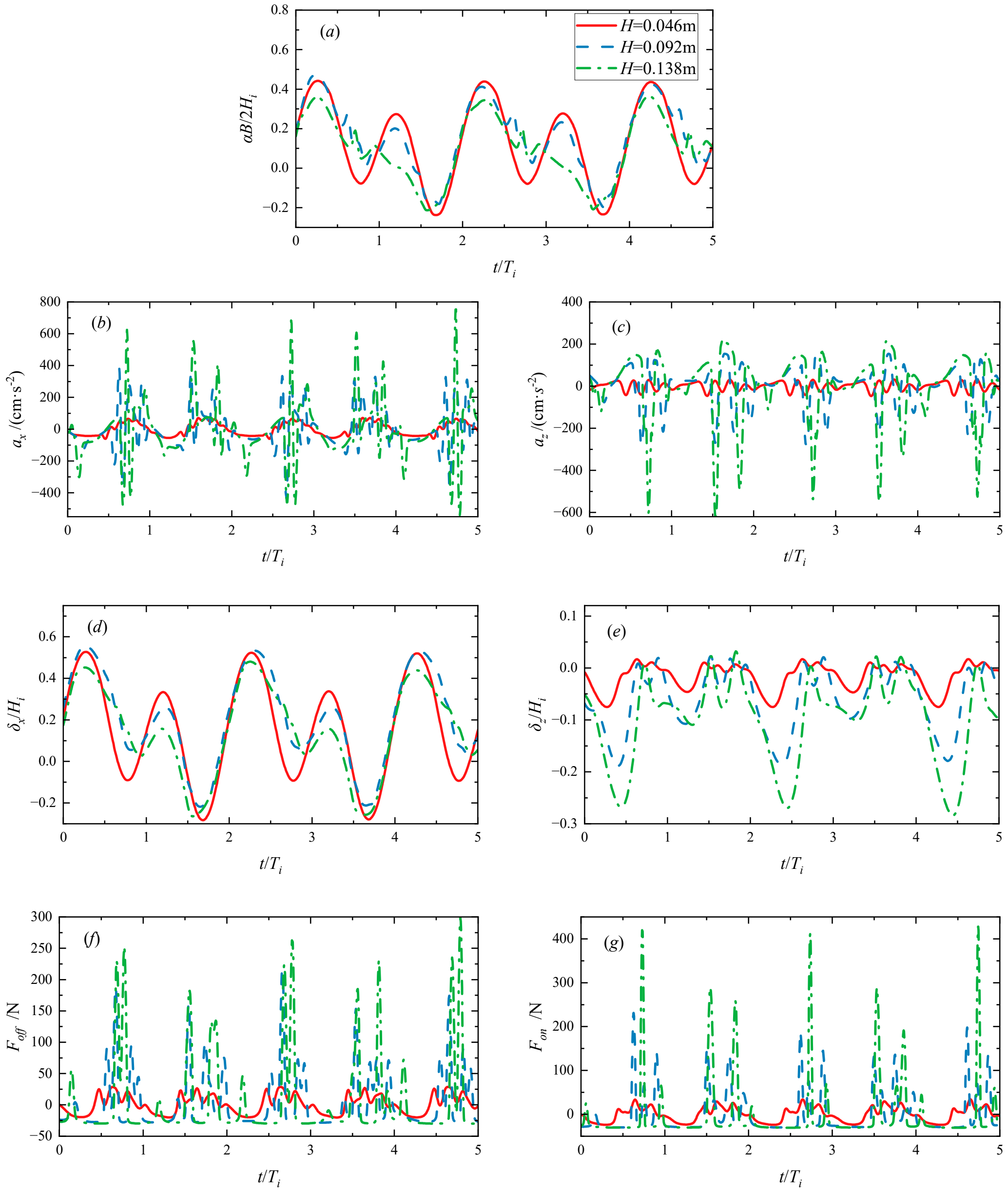

Figure 6. Time series of the dynamic response of SFT under wave load. (**a**) Roll of the SFT (**b**) Horizontal directional acceleration of the SFT (**c**) Vertical directional acceleration of the SFT (**d**) Sway of the SFT (**e**) Heave of the SFT (**f**) Offshore tension of the anchor cable (**g**) Onshore tension of the anchor cable.

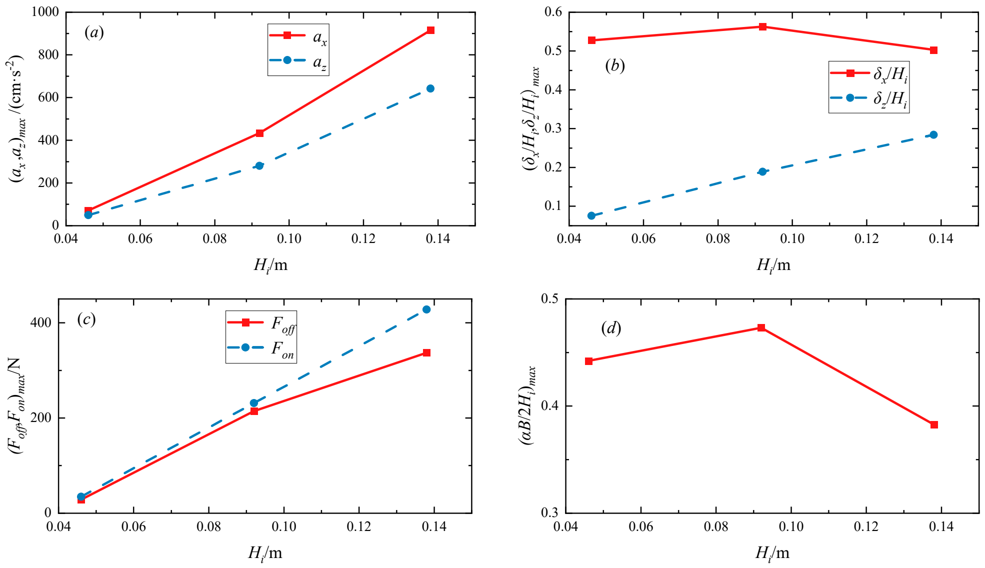

Figure 7. Variation of the maximum response value of SFT with wave height. (**a**) Maximum values of horizontal and vertical directional accelerations of the SFT (**b**) Maximum values of sway and heave of the SFT (**c**) Maximum values of the offshore and onshore tensions of the anchor cable (**d**) Maximum value of roll of the SFT.

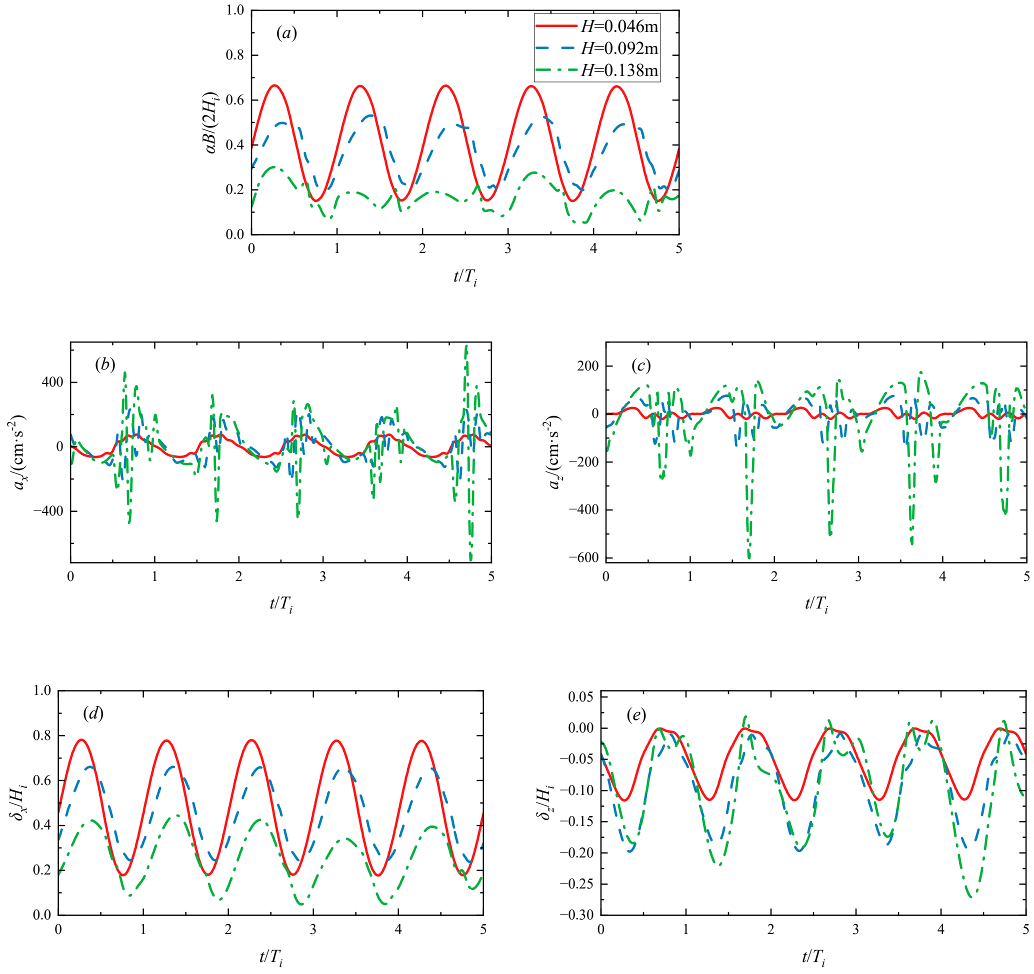

Figure 8. *Cont*.

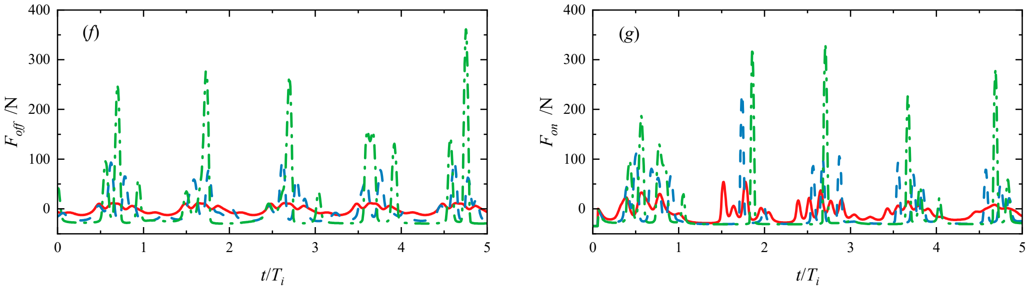

Figure 8. Time series of responses at different wave heights and in the same direction of wave and flow. (**a**) Roll of the SFT (**b**) Horizontal directional acceleration of the SFT (**c**) Vertical directional acceleration of the SFT (**d**) Sway of the SFT (**e**) Heave of the SFT (**f**) Offshore tension of the anchor cable (**g**) Onshore tension of the anchor cable.

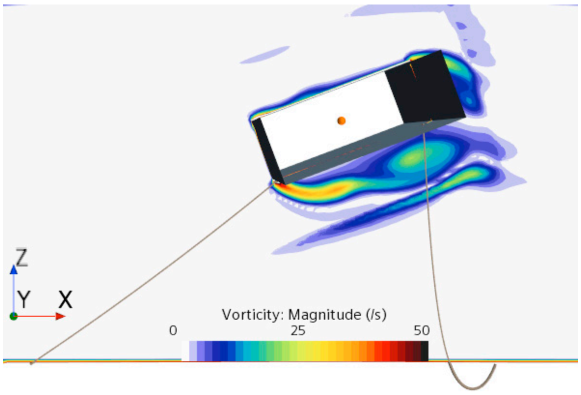

Figure 9. Periodic shedding of vortices from the surface of the SFT.

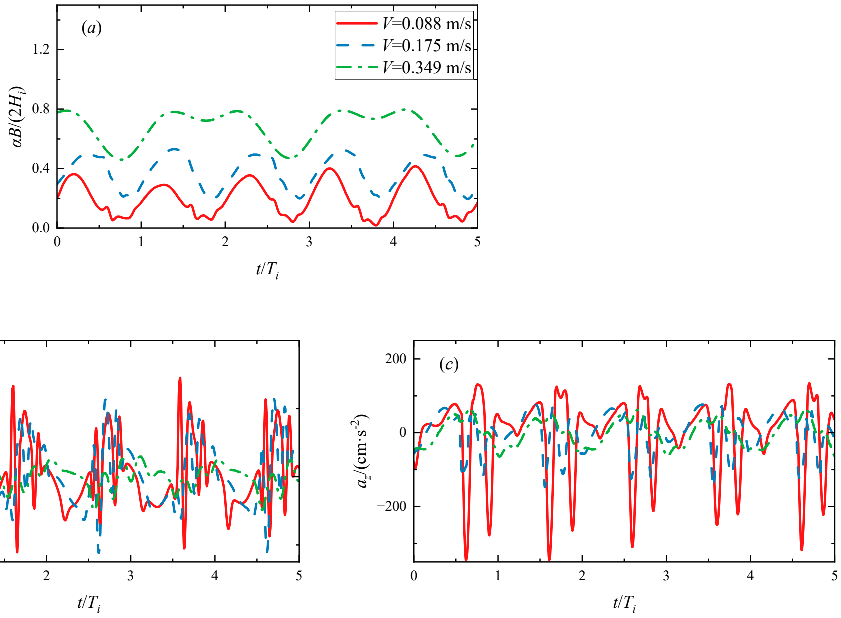

Figure 10. *Cont.*

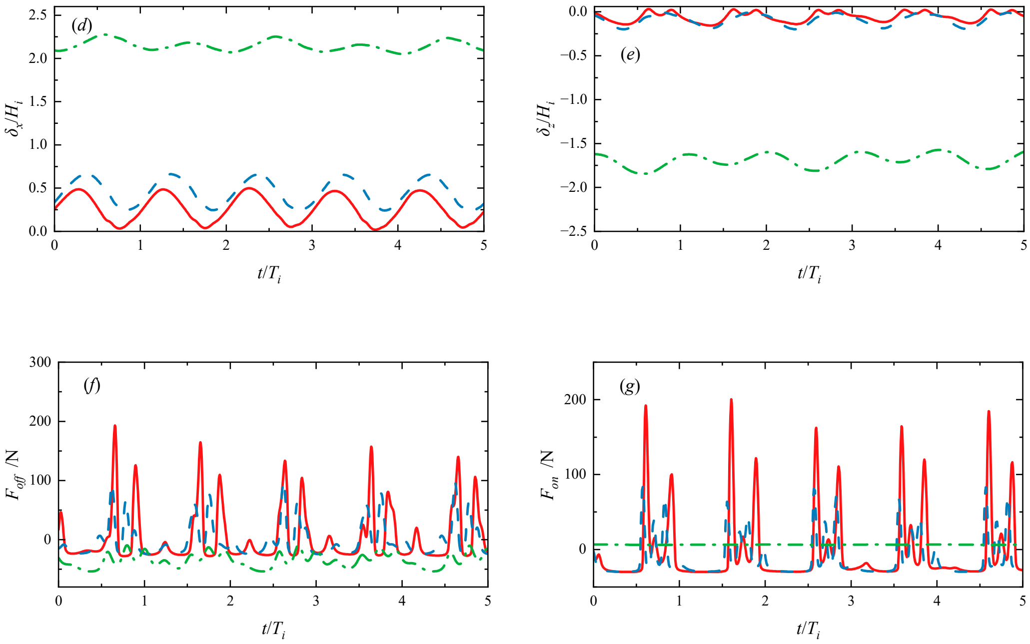

Figure 10. Time series of responses at different flow velocities and in the same direction of wave and flow. (**a**) Roll of the SFT (**b**) Horizontal directional acceleration of the SFT (**c**) Vertical directional acceleration of the SFT (**d**) Sway of the SFT (**e**) Heave of the SFT (**f**) Offshore tension of the anchor cable (**g**) Onshore tension of the anchor cable.

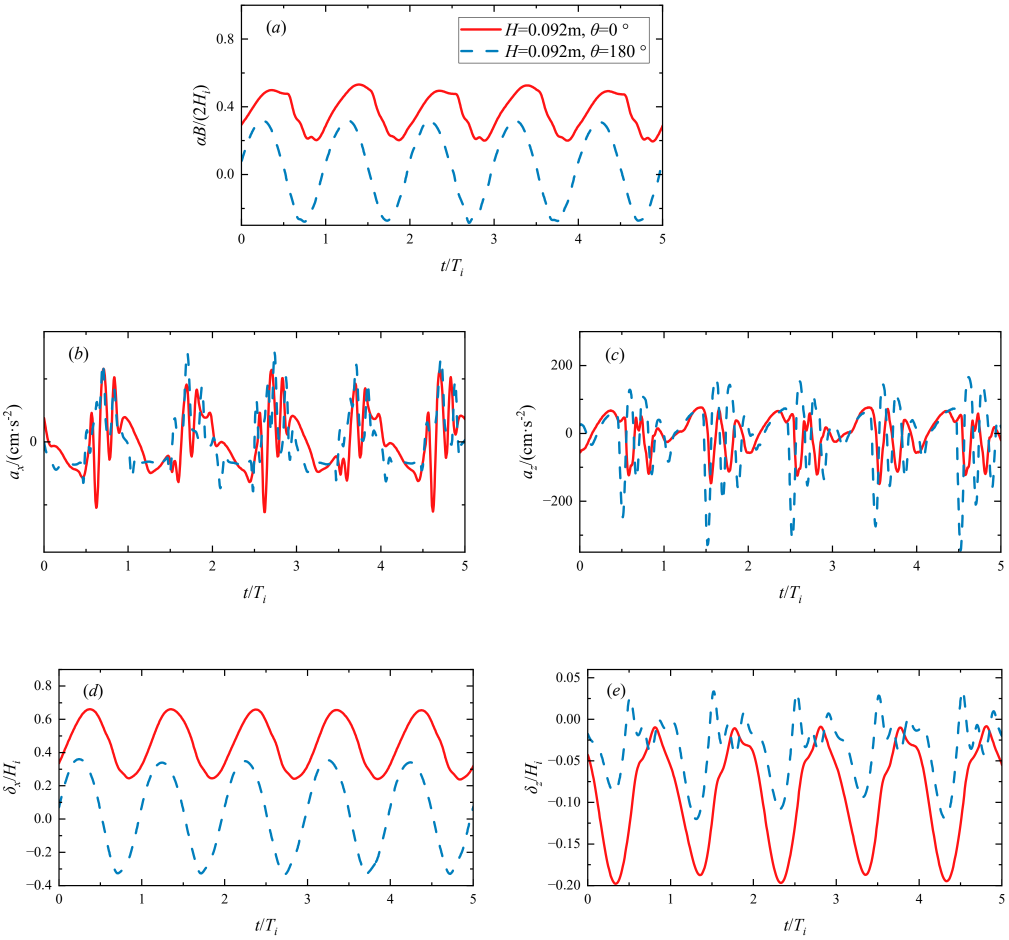

Figure 11. *Cont.*

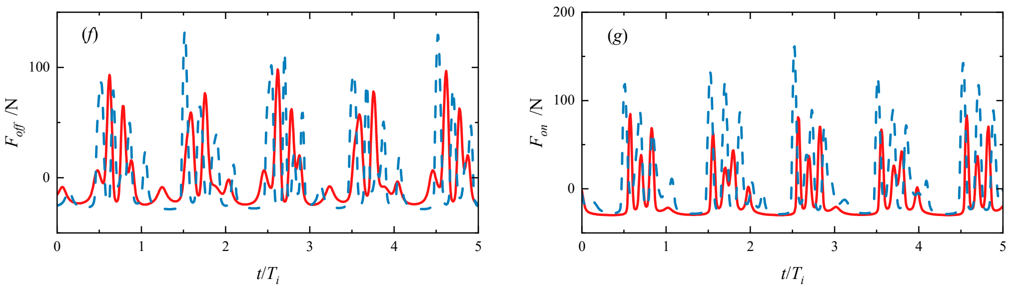

Figure 11. Comparison of responses of SFT in the same and reverse directions of wave and flow. (**a**) Roll of the SFT (**b**) Horizontal directional acceleration of the SFT (**c**) Vertical directional acceleration of the SFT (**d**) Sway of the SFT (**e**) The heave of the SFT (**f**) Offshore tension of the anchor cable (**g**) Onshore tension of the anchor cable.

5. Conclusions

A numerical computational model was established to simulate the system comprising SFT and anchor chains. The accuracy of the numerical model was validated through comparison with model test results. The influence of parameters such as wave height, flow velocity, and wave and flow propagation direction on the dynamic response of the SFT was analyzed. The main conclusions are as follows:

Under the isolated action of a wave, an increase in wave height leads to a significant increase in the maximum values of a_x, a_z, F_{off}, F_{on}, and δ_z/H_i, accompanied by an augmentation in the nonlinear characteristics. While wave height variation does not significantly affect δ_x/H_i, the maximum value of $\alpha B/(2H_i)$ initially increases and then decreases with increasing wave height.

When waves and flows propagate in the same direction with a fixed flow velocity, the effects of wave height on the SFT are similar to those observed under isolated wave conditions. An increase in wave height results in larger maximum values for a_x, a_z, F_{off}, F_{on}, and δ_z/H_i, while δ_x/H_i and $\alpha B/(2H_i)$ decrease. Moreover, under combined wave and flow propagation, the δ_z/H_i for the SFT increases for all wave heights compared to cases with regular waves acting alone, while δ_x/H_i and $\alpha B/(2H_i)$ exhibit smaller vibration amplitudes. The presence of flow causes the equilibrium position of the lateral motion of the SFT to shift along the direction of wave and flow propagation, with this displacement influenced by wave height. Notably, higher wave heights lead to smaller lateral vibration amplitudes. Additionally, the SFT rotates a certain angle against the incoming flow and then undergoes periodic rotational motion at the new position. Similarly, as wave height increases, the angle of counterclockwise rotation diminishes. As wave height increases, the non-linear characteristics of the pitch motion of the SFT amplify.

When waves and flows propagate in the same direction with a fixed wave height under the condition of relatively high flow velocity, the SFT displaces significantly in both the direction of flow and the depth of the water, causing it to deviate considerably from its original equilibrium position. At this juncture, the SFT is largely unaffected by wave loads and predominantly experiences periodic lift and drag forces resulting from vortex shedding along the tunnel's surface. On the side opposite the flow, the anchor chain remains completely slack.

When waves and flows propagate in opposite directions, the maximum values of a_x, a_z, F_{on}, and F_{off} for the SFT exhibit significant increases. Structural considerations are required in the design process to prevent anchor chain rupture.

Author Contributions: Conceptualization, methodology, software, W.X. and Z.S.; Validation, formal analysis, and investigation, G.L. and Y.S. All authors have read and agreed to the published version of the manuscript.

Funding: This research was funded by the National Natural Science Foundation of China (U2106223 and 51979163).

Conflicts of Interest: The authors declare no conflict of interest.

References

1. Hou, Z.-Y. *The Models for Hydrodynamic Analysis of the Submerged Floating Tunnel under Wave and Current Action*; Dalian University of Technology: Dalian, China, 2020.
2. Zhong, D.; Li, K.; Sun, M.-G. Research progress on hydrodynamic characteristics and model test of submerged floating tunnel in China. *Technol. Highw. Transp.* **2023**, *39*, 133–141.
3. Xu, W.; Ma, Y.; Liu, G.; Li, M.; Li, A.; Jia, M.; He, Z.; Du, Z. A review of research on tether-type submerged floating tunnels. *Appl. Ocean Res.* **2023**, *134*, 103525. [CrossRef]
4. Fan, Z.-X.; Yuan, Y.; He, R.-F.; Zhang, J.-W.; He, W.-G. Dynamic response analysis of submerged floating tunnel supported on columns in vortex-induced vibration. *J. Railw. Sci. Eng.* **2020**, *17*, 653–659.
5. Ge, F.; Lu, W.; Wu, X.; Hong, Y. Fluid-structure interaction of submerged floating tunnel in wave field. *Procedia Eng.* **2010**, *4*, 263–271. [CrossRef]
6. Kunisu, H. Evaluation of wave force acting on Submerged Floating Tunnels. *Procedia Eng.* **2010**, *4*, 99–105. [CrossRef]
7. Mai, J.; Yang, X.; Guo, B. Calculations of the wave loads on submerged floating tunnels. *J. Rail Way Sci. Eng.* **2007**, *4*, 83–87.
8. Tian, X.F.; Dong, M.S.; Pang, H.P.; Lin, Z.; Niu, Z. Dynamic responses of the submerged floating tunnel under combined internal wave and sea current effect. *Appl. Math. Mech.* **2014**, *35*, 71–80.
9. Morison, J.R.; Johnson, J.W.; Schaaf, S.A. The force exertend by surface waves on piles, petroleum trans. *J. Pet. Technol.* **1950**, *2*, 149–154. [CrossRef]
10. Yang, Z.; Li, J.; Zhang, H.; Yuan, C.; Yang, H. Experimental Study on 2D Motion Characteristics of Submerged Floating Tunnel in Waves. *J. Mar. Sci. Eng.* **2020**, *8*, 123. [CrossRef]
11. Kim, G.J.; Lee, S.; Kim, M.; Kwak, H.G.; Hong, J.W. Characterization of single and dual SFT through a hydraulic experiment under regular and irregular waves. *Ocean Eng.* **2022**, *263*, 112365. [CrossRef]
12. Li, Q.-X. *Numerical Simulation and Physical Experiment of Submerged Floating Tunnel Key Parameters under Wave-Current Coupling*; Chongqing Jiaotong University: Chongqing, China, 2019.
13. Wang, F.; Li, K.; Huang, B.; Cheng, L.; Ding, H. Experimental Investigation of the Dynamic Behavior of Submerged Floating Tunnels under Regular Wave Conditions. *J. Mar. Sci. Eng.* **2022**, *10*, 1623. [CrossRef]
14. Yang, S.; Hu, Q.-Y.; Wu, Z.-W.; Mou, L.-W.; Wei, C.-X. Dynamic Response for Submerged Floating Tunnel during Local Anchor Cable Breakage under Wave and Current Load. *Ship Eng.* **2021**, *43*, 149–154.
15. Zou, P.-X.; Liu, M.-Y.; Chen, L.-Z. Study on the Hydrodynamic Characteristics of the Coupling System of Submerged Floating Tunnel Tubes and Anchor Cables under Wave Action. *Mod. Tunn. Technol.* **2021**, *58*, 154–162.
16. Luo, W.; Huang, B.; Tang, Y.; Ding, H.; Li, K.; Cheng, L.; Ren, Q. Numerical Simulation of Dynamic Response of Submerged Floating Tunnel under Regular Wave Conditions. *Shock Vib.* **2022**, *2022*, 1–15. [CrossRef]
17. Zou, P.X.; Bricker, J.D.; Chen, L.Z.; Uijttewaal, W.S.; Ferreira, C.S. Response of a submerged floating tunnel subject to flow-induced vibration. *Eng. Struct.* **2022**, *253*, 113809. [CrossRef]
18. Chen, X.; Chen, Q.; Chen, Z.; Cai, S.; Zhuo, X.; Lv, J. Numerical modeling of the interaction between submerged floating tunnel and surface waves. *Ocean Eng.* **2021**, *220*, 108494. [CrossRef]
19. Peng, W.; Lee, K.H.; Shin, S.H.; Mizutani, N. Numerical simulation of interactions between water waves and inclined-moored submerged floating breakwaters. *Coast. Eng.* **2013**, *82*, 76–87. [CrossRef]
20. Wang, F.-J. *Principles and Applications of Computational Fluid Dynamics (CFD) Software in Fluid Dynamics Analysis*; Tsinghua University Press: Beijing, China, 2004. (In Chinese)
21. Kim, J.; O'Sullivan, J.; Read, A. Ringing Analysis of a Vertical Cylinder by Euler Overlay Method. In Proceedings of the International Conference on Offshore Mechanics and Arctic Engineering, OMAE, Rio de Janeiro, Brazil, 1 July 2012; American Society of Mechanical Engineers: New York, NY, USA, 2012.
22. CD-Adapco. STAR-CCM+ Version 11.04 Manual [EB/OL]. 2016. Available online: https://support.sw.siemens.com/en-US/ (accessed on 1 July 2016).